

A simple model for laser drilling

Jeb Collins^{a,1}, Pierre Gremaud^{b,2,*}

^a*Department of Mathematics, North Carolina State University, Raleigh, NC
27695, USA*

^b*Department of Mathematics, North Carolina State University, Raleigh, NC
27695, USA and Statistical and Applied Mathematical Sciences Institute (SAMSI),
P.O. Box 14006, Research Triangle Park, NC 27709-4006, USA*

Abstract

A simple mathematical model of laser drilling is proposed. Assuming axi-symmetry of the process around the axis of the laser beam, a one-dimensional formulation is obtained after cross-sectional averaging. The novelty of the approach relies on the fact that even after dimension reduction, the shape of the hole can still be described. The model is derived, implemented and validated for drilling using lasers with intensities in the GW/cm² range and microsecond pulses.

Key words: laser drilling, phase change, free boundary, numerical methods

1 Introduction

Laser drilling is an important industrial process by which laser pulses are used to drill holes in hard materials. It presents several advantages over conventional techniques such as low heat input into the material, accuracy, consistency, ease to automate and ability to drill very small holes of the order of 10 microns in diameter. This technique is used either with single or multiple pulses.

* Corresponding author.

Email addresses: jbcoll12@ncsu.edu (Jeb Collins), gremaud@ncsu.edu (Pierre Gremaud).

¹ Partially supported by the National Science Foundation (NSF) through grants DMS-0636590 and DMS-0811150

² Partially supported by the National Science Foundation (NSF) through grants CMMI-0738044, DMS-0636590 and DMS-0811150

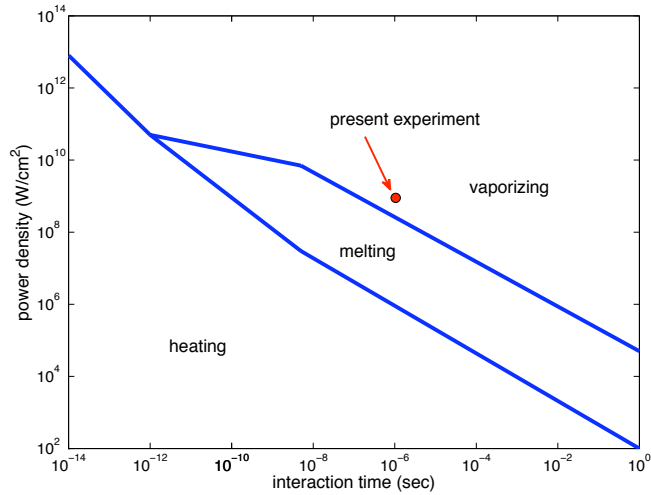


Fig. 1. Approximate range of various regimes for laser ablation (adapted from [9]).

During drilling, material is removed from the workpiece through two mechanisms: vaporization and melt ejection. The relative importance of each mechanism has been the object of several theoretical studies, see for instance [13]. Some authors have also developed more phenomenological criteria [9], see Figure 1. In the case of thermal ablation (roughly the lower left part of Figure 1), the interaction of the laser with the material surface creates a molten pool. As some of the material vaporizes, the pressure of the vapor (recoil pressure) is large enough to push the melt radially outward from the center of the beam, leading to melt ejection. On the other hand, in so-called non-thermal ablation (roughly the upper right part of Figure 1), which corresponds to higher melt surface temperature, the main process by which melt is removed is through evaporation instead of convection as the material vaporizes before it can get convected in any significant way.

The mechanisms involved in laser drilling have been described by previous authors [1,7,8,11,13,15,16] to cite but a few. The main contribution of the present paper is the construction and implementation of a new simple model to predict penetration depth and hole diameter in a specific regime corresponding to a relatively powerful laser, with power density in the GW/cm^2 range, used in conjunction with microsecond pulses, see Section 4 for details, see also [5] for general remarks on this regime. Figure 1 illustrates where the case(s) considered here stand(s) in relation with other applications; see for instance [4,12] for recent models dealing with TW/cm^2 power densities and pico or femto second pulses.

Many practical questions remain open such as the determination of optimal firing schedules or the mitigation of instabilities leading to poor quality holes. Our approach leads to a model amenable to either optimization or stability studies. The proposed model is based on several simplifying assumptions

which are detailed in Section 2. The process is also considered to be fully axisymmetric along the axis of the laser beam. The model is made pseudo one-dimensional through the use of a cross-sectional averaging. However, in the present model, various polynomial hole shapes can still be considered. The aspect ratio is a model parameter that is determined based on the available experimental data. Implementation is described in Section 3. Our results are discussed in Section 4 together with comparison with experimental data.

2 Mathematical modeling

2.1 Heat transfer

We assume the workpiece to be homogenous and the laser beam to have a Gaussian intensity distribution. Under these conditions, the entire process can be considered axi-symmetric. Working with a cylindrical coordinate system (r, θ, z) centered on the laser with z pointing down, energy conservation takes the form the classical heat equation

$$\rho_s c_s \frac{\partial T}{\partial t} = k_s \left[\frac{1}{r} \frac{\partial}{\partial r} \left(r \frac{\partial T}{\partial r} \right) + \frac{\partial^2 T}{\partial z^2} \right] \quad r > 0, z > 0, t > 0, \quad (1)$$

where T is the temperature, ρ_s , c_s and k_s are respectively the density, heat capacity and thermal conductivity of the solid material and are in first approximation considered constant. If W stands for the intensity or power flux of the laser, we have in the first stages of the process

$$k_s \frac{\partial T}{\partial z} = -W. \quad \text{at } z = 0. \quad (2)$$

Typical values for the above parameters are given in Table 1. It is important to note that vertical and radial diffusions play very different roles for the regime in which we operate. This can be seen by non-dimensionalizing the above equation. To this end, we introduce r^* , z^* and t^* typical values of respectively r , z and the time t

$$r^* = R_b, \quad z^* = \frac{k(T_v - T_m)}{W}, \quad t^* = \rho_s c_s k_s \frac{(T_v - T_m)^2}{W^2},$$

where R_b is the diameter of the beam, and T_m and T_v are respectively the melting and vaporization temperature, see again Table 1. We now rewrite (1) in terms the non-dimensional variables

$$\bar{r} = \frac{r}{R_b}, \quad \bar{z} = \frac{z}{z^*}, \quad \bar{T} = \frac{T - T_m}{T_v - T_m},$$

and get, omitting the bars

$$\frac{\partial T}{\partial t} = \epsilon \frac{1}{r} \frac{\partial}{\partial r} \left(r \frac{\partial T}{\partial r} \right) + \frac{\partial^2 T}{\partial z^2},$$

where

$$\epsilon = k_s^2 \frac{(T_v - T_m)^2}{R_b^2 W^2} \approx 10^{-8}.$$

Radial diffusion plays therefore a secondary role. Based on this, we construct a family of pseudo one-dimensional models obtained from radial averaging. More precisely, let $s(z, t)$ be the assumed radius of the hole at depth z and time t and let $\xi(t)$ be the maximal depth of the hole at time t , i.e., the depth along the z -axis. Three different following profiles are implemented, see Figure 2

- constant profile $s_\infty(z, t) = \begin{cases} \kappa_\infty \xi(t) & \text{if } z < \xi(t), \\ 0 & \text{if } z \geq \xi(t), \end{cases}$
- conical profile $s_1(z, t) = \begin{cases} \kappa_1(\xi(t) - z) & \text{if } z < \xi(t), \\ 0 & \text{if } z \geq \xi(t), \end{cases}$
- parabolic profile $s_2(z, t) = \begin{cases} \kappa_2 \sqrt{\xi(t)^2 - \xi(t)z} & \text{if } z < \xi(t), \\ 0 & \text{if } z \geq \xi(t). \end{cases}$

Defining more generally

$$s_\ell(z, t) = \begin{cases} \kappa_\ell \left(\xi(t)^\ell - \xi(t)^{\ell-1} z \right)^{1/\ell} & \text{if } z < \xi(t), \\ 0 & \text{if } z \geq \xi(t), \end{cases}$$

the case of the piecewise constant profile s_∞ can be viewed as a singular limit of the other cases

$$s_\infty(z, t) = \lim_{\ell \rightarrow \infty} s_\ell(z, t).$$

For future reference, we denote by R the radius of the hole at $z = 0$, i.e., we set $R(t) = s(0, t)$. The aspect ratios κ_∞ , κ_1 and κ_2 are considered constant; proper corresponding values will be determined below.

In agreement with Figure 1, we consider only the vaporization process. Numerical tests were ran with and without liquefaction and confirmed the very secondary role played by it in the present context. The boundary condition corresponding to the phase change is a Stefan-like boundary condition. More precisely, on the interface, i.e., for $(r, z) = (\rho(z, t), z)$, we have

$$k_s \nabla T \cdot n = -W n_z + \rho_s L_v u \cdot n, \quad (3)$$

where L_v is the latent heat of vaporization, n is the unit normal vector to the interface into the solid and u is the local velocity of the interface at the

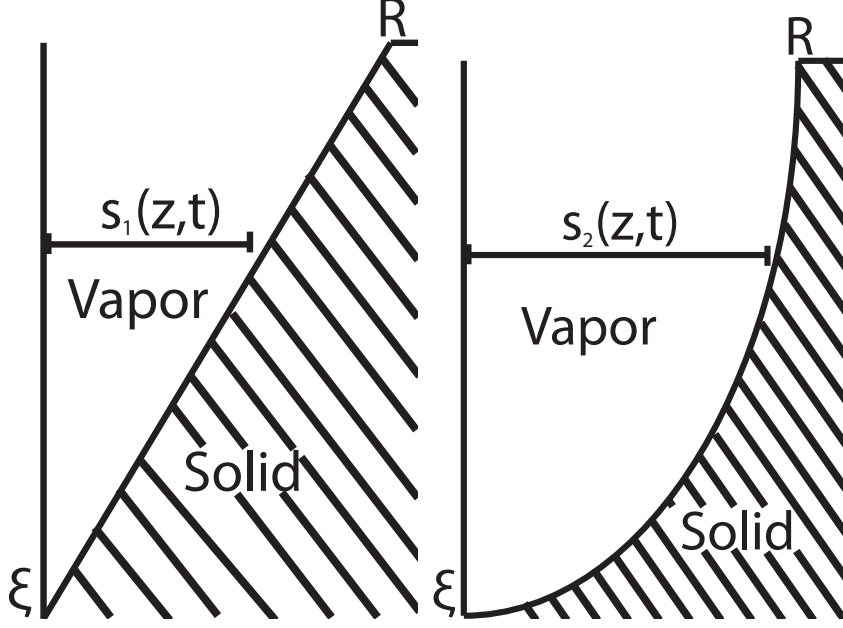


Fig. 2. Assumed hole shapes; left: cone, right: paraboloid.

considered point. The evaluation of u is delicate in the present framework as there is no obvious way to track a material point on the interface. In other words, there are many ways to map the interface at time t , i.e.,

$$\{(r, z); 0 < z < \xi(t), r = s(z, t)\},$$

to the interface at time $t + dt$. In first approximation, we choose to neglect the radial component of the local velocity in the Stefan condition (3). More precisely, consider a point on the interface at time t with coordinates $(r(t), z(t))$ where r and z are related by

$$r - s_\ell(z, t) = 0, \quad (4)$$

which can be equivalently expressed as

$$z = \xi(t) - \frac{1}{\kappa_\ell^\ell} \frac{r^\ell}{\xi(t)^{\ell-1}}. \quad (5)$$

Under the above assumptions, the velocity u of the considered interface point (r, z) is then approximated by

$$u \approx [0, \dot{z}] \approx \left[0, \dot{\xi} \left(1 + (\ell - 1) \left(\frac{r}{\kappa \xi} \right)^\ell \right) \right] \equiv [0, u_z], \quad (6)$$

where the last expression corresponds to the time derivative of (5), neglecting the radial contribution.

Following the above remark on radial vs. vertical diffusion, we neglect the r dependencies in (3) and obtain

$$k_s \frac{\partial T}{\partial z}(s(z, t), z, t) = -W + \rho_s L_v u_z. \quad (7)$$

For any axi-symmetric field $V(r, \theta, z, t) = V(r, z, t)$ defined in the computational domain, we denote by \bar{V} the corresponding radially averaged field

$$\bar{V}(z, t) = \frac{2}{R(t)^2 - s(z, t)^2} \int_{s(z, t)}^{R(t)} V(r, z, t) r dr.$$

By applying averaging to (1) and neglecting the terms $\bar{T} - T(s(z, t), z, t)$ and $\bar{T} - T(R, z, t)$, we obtain after some algebra

$$\frac{\partial \bar{T}}{\partial t} = \alpha \left(\frac{\partial^2 \bar{T}}{\partial z^2} - \frac{4 s s'}{R^2 - s^2} \left(\frac{\partial \bar{T}}{\partial z} - \frac{\partial T(s, z, t)}{\partial z} \right) \right) \quad z > 0, t > 0,$$

where $\alpha = \frac{k_s}{\rho_s c_s}$, $\frac{\partial T}{\partial z}$ is defined in (7) and s' denotes the spatial (z) derivative of s . The full averaged problem becomes

$$\frac{\partial \bar{T}}{\partial t} = \alpha \left(\frac{\partial^2 \bar{T}}{\partial z^2} - \frac{4 s s'}{R^2 - s^2} \left(\frac{\partial \bar{T}}{\partial z} + \frac{1}{k_s} (W - \rho_s L_v u_z) \right) \right), \quad z > 0, t > 0, \quad (8)$$

$$k_s \frac{\partial \bar{T}}{\partial z} = -W + \rho_s L_v u_z, \quad z = 0, t > 0, \quad (9)$$

$$\lim_{z \rightarrow \infty} \bar{T} = T_0, \quad t > 0, \quad (10)$$

$$\bar{T}(\cdot, 0) = T_0, \quad z > 0, \quad (11)$$

where the boundary condition (9) results from the right hand side of (7) being independent of z and where T_0 is the ambient temperature. In the singular limit corresponding to the piecewise constant profile ρ_∞ , equations (8) and (9) take the form

$$\frac{\partial \bar{T}}{\partial t} = \alpha \frac{\partial^2 \bar{T}}{\partial z^2}, \quad z > \xi(t), t > 0, \quad (12)$$

$$k_s \frac{\partial \bar{T}}{\partial z} = -W + \rho_s L_v u_z, \quad z = \xi(t), t > 0. \quad (13)$$

2.2 Knudsen layer jump conditions

The high power of the laser results in rapid evaporation of the workpiece. While the vapor near the evaporation interface is not in thermal equilibrium, it reaches thermal equilibrium after only a few mean free paths. This thin layer out of thermal equilibrium is called the Knudsen layer. The lack of equilibrium

implies that the state variables change quickly in that region. Following [8], we assume the Knudsen layer to be infinitesimally thin and that the state variables jump between the solid and vapor side of the Knudsen layer .

Mass, momentum and energy must be conserved across the Knudsen layer. Further, by assuming the vapor to have a half Maxwellian distribution function and all back-scattered particles to condense, jump conditions for the temperature and density can be derived, see [8] for full details

$$\sqrt{\frac{T_*}{T_s}} = \sqrt{1 + \pi \left(\frac{m(\gamma - 1)}{2(\gamma + 1)} \right)^2} - \sqrt{\pi} \frac{m(\gamma - 1)}{2(\gamma + 1)}, \quad (14)$$

$$\frac{\rho_*}{\rho_e} = \frac{F^- + \sqrt{\frac{T_*}{T_s}} G^-}{2e^{-m^2} \frac{T_*}{T_s}}, \quad (15)$$

where T_* and ρ_* are the temperature and density on the vapor side of the Knudsen layer while T_s is the temperature of the workpiece near the Knudsen layer determined from the heat transfer problem; ρ_e , which depends on T_s , is the saturation density and is discussed below. We assume the metal vapor is to be monatomic and thus the ratio of specific heat in the vapor, γ has value 1.67; in the ambient air, that value is $\gamma = 1.4$ [10]. The extra parameter in (14) and (15) is the dimensionless evaporation rate m . Finally, the two auxiliary functions F^- and G^- are defined by

$$F^- = e^{-m^2} - \sqrt{\pi} m \operatorname{erfc}(m), \quad (16)$$

$$G^- = (2m^2 + 1) \operatorname{erfc}(m) - \frac{2}{\sqrt{\pi}} m e^{-m^2}. \quad (17)$$

The saturation pressure p_e can be related to the surface temperature T_s through the Clausius-Clapeyron relation [2]

$$p_e = p_1 \exp \left(\frac{L_v}{\mathcal{R}_1} \left(\frac{1}{T_s} - \frac{1}{T_1} \right) \right), \quad (18)$$

where T_1 is the value of T_s required to produce a vapor pressure of p_1 , the ambient pressure and \mathcal{R}_1 is the specific gas constant, i.e., $\mathcal{R}_1 = R/M_{\text{mol},1}$ where R is the universal gas constant and $M_{\text{mol},1}$ is the molar mass of the considered gas. Here, we use the ambient air, region 1 in Figure 3, as a reference state. Using the ideal gas law, p_e can then related to ρ_e , i.e.

$$p_e = \rho_e \mathcal{R}_3 T_s. \quad (19)$$

Even together with (18) and (19), the jump relations (14) and (15) are not enough to determine T_*, ρ_* , on the vapor side of the Knudsen layer, given

similar data on the solid side since they contain the unknown dimensionless evaporation rate m . We close the system by considering the Euler equations of gas dynamics in the vapor [1,8,10]

$$\begin{aligned}\partial_t \rho + \partial_z(\rho u) &= 0, \\ \partial_t(\rho u) + \partial_z(\rho u^2 + p) &= 0, \\ \partial_t E + \partial_z((E + p)u) &= 0,\end{aligned}$$

where ρ is the density of the vapor, u its velocity and $p = p(\rho, E)$ its pressure; E is the total energy. Kinetic theory does not allow the vapor near the Knudsen layer to be supersonic [16].

This implies that we must use two cases to solve for the states, one when the vapor is subsonic or sonic and one when it is supersonic. In the subsonic case, the vapor can be represented by the diagram in Figure 3, left, and we can close our system for m by invoking the Rankine-Hugoniot jump conditions of the Euler gas dynamics equations. In the supersonic case, the vapor is represented by Figure 3, right. In that case, a rarefaction wave takes the vapor from the sonic state at the Knudsen layer to a supersonic state away from the Knudsen layer. To close the system in the supersonic case we must use both the Riemann invariants across the rarefaction fan and the Rankine-Hugoniot conditions. As shown in Figure 9 from Section 4, the supersonic case applies during most of the experiment simulated here.

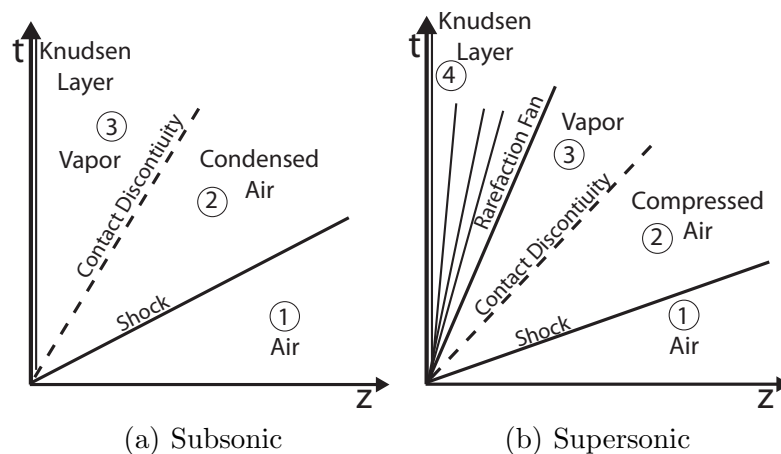


Fig. 3. Diagrams of gas regions.

Starting with the subsonic case, Figure 3 shows that the gas has three regions that are separated by a contact discontinuity and a shock. The region closest to the Knudsen layer, which we have labeled 3, is vapor. Region 2 is also compressed air, and is separated from region 3 by a contact discontinuity, i.e., both the pressure and velocity are equal in region 2 and 3

$$p_2 = p_3 \quad \text{and} \quad u_2 = u_3.$$

Region 1 is ambient air, which is separated from the compressed air by a shock wave. The final equation, to close the system for m , is obtained from the Rankine-Hugoniot jump condition across this shock wave. After much algebraic manipulations, we obtain

$$\frac{p_3}{p_1} = 1 + \gamma_1 \sqrt{\frac{2}{\gamma_3}} \frac{c_3}{c_1} m \left[\frac{m}{2\sqrt{2}} \frac{\gamma_1 + 1}{\sqrt{\gamma_3}} \frac{c_3}{c_1} + \sqrt{1 + \frac{2}{\gamma_3} \left(\frac{\gamma_1 + 1}{4} \frac{c_3}{c_1} m \right)^2} \right] \quad (20)$$

where $c_i = \sqrt{\gamma_i \mathcal{R}_i T_i}$ is the speed of sound and the subscripts indicate the region the variable represents. The value of p_1 is known since it is the pressure of the ambient air. The ideal gas law yields

$$\frac{p_3}{p_e} = \frac{\rho_3}{\rho_e} \frac{T_3}{T_s}. \quad (21)$$

Using (14), (15), (18) and (20) to respectively express the ratios $\frac{T_3}{T_s}$, $\frac{\rho_3}{\rho_e}$, $\frac{p_1}{p_e}$ and $\frac{p_3}{p_1}$, relation (21) results in an equation containing only the unknown dimensionless evaporation rate m and T_s which we assume known at this stage.

In the supersonic case, as shown in Figure 3, most of the structure of the gas dynamics is the same, except for the creation of an additional region after the rarefaction fan. The region near the Knudsen layer, now labeled 4, is sonic and so we can determine all of the states in this region by letting $m = \sqrt{\gamma_3}/2$, which corresponds to a Mach number of one. The states we are now looking for are those downwind of the rarefaction fan. Using Riemann invariants from the Euler gas dynamics equations, which are constant throughout a rarefaction wave, we gain a relationship between p_3 and p_4 ,

$$\frac{p_4}{p_3} = \left(\frac{c_4}{c_3} \right)^{2\gamma_3/(\gamma_3-1)} = \left(\frac{\sqrt{2}}{\gamma_3 + 1} \left(\sqrt{2} + \frac{\gamma_3 - 1}{\sqrt{\gamma_3}} m \right) \right)^{2\gamma_3/(\gamma_3-1)}. \quad (22)$$

Equation (20) still holds because the relationships between region 1, 2 and 3 are unchanged. In the present supersonic case, however, the sound speed c_3 cannot be derived from (14) since region 3 is no longer at the Knudsen layer. Since region 4 is sonic, the corresponding state can be determined and consequently, the value of c_3 can be obtained from

$$\frac{c_3}{c_1} = \sqrt{\frac{\gamma_3 R_3 T_s T_4}{\gamma_1 R_1 T_1 T_s}} \left(\frac{c_4}{c_3} \right)^{-1},$$

together with (22). Finally, similarly to the subsonic case, we obtain a nonlinear equation for m by expressing the ratios in the trivial relation

$$\frac{p_e}{p_1} = \frac{p_4}{p_3} \frac{p_3}{p_1} \left(\frac{p_4}{p_e} \right)^{-1}, \quad (23)$$

using the above remarks.

Once we solve for m , we calculate the thermodynamic state variables T_g and ρ_g on the vapor side of the Knudsen layer which will be used in the update of the interface speed.

2.3 Interface Speed Update

The final component in our model is the update of the speed $U = \dot{\xi}$ of the interface. Using the continuity equation and the assumption that the distribution function for the vapor is Maxwellian, one obtains [16].

$$U = \frac{1}{\rho_s} \left[\rho_e \sqrt{\frac{T_s \mathcal{R}}{2\pi}} - \rho_g \sqrt{\frac{T_g \mathcal{R}}{2\pi}} F^- \beta(m) \right], \quad (24)$$

where

$$\beta(m) = \frac{2(2m^2 + 1) \sqrt{\frac{T_*}{T_s}} - 2\sqrt{\pi} m}{F^- + \sqrt{\frac{T_*}{T_s}} G^-}$$

ρ_e is the saturation density, T_g and ρ_g are the vapor temperature and density calculated from the Knudsen layer jump conditions, and T_s is the temperature of the workpiece near the Knudsen layer.

3 Implementation

The implementation follows the previous section as shown in Figure 3. The process is started with initial values for the temperature field, T_0 , the speed of the interface U and the velocity of the vapor. Of these, only T_0 has an essential meaning, the other two being numerical auxiliary quantities. To advance the solution by $\Delta t > 0$ in time, the following steps are considered.

Step 1 Given U and the current temperature T^n , we solve for T^{n+1} , solution to the heat transfer problem ((8)-(11) or (12), (13), (10), (11) for $\ell \rightarrow \infty$) from time t to $t + \Delta t$ with initial condition $T_0 = T^n$. The value T_s is obtained by averaging T^{n+1} over the free boundary.

Step 2 Given T_s and the current velocity of the gas to determine whether the flow is subsonic or supersonic, we solve the Knudsen layer jump condition, i.e., either (21) or (23), for m .

Step 3 Given m , the state variables for the vapor can be computed and $\mathfrak{F}(U)$, the right hand side of (24), can be evaluated.

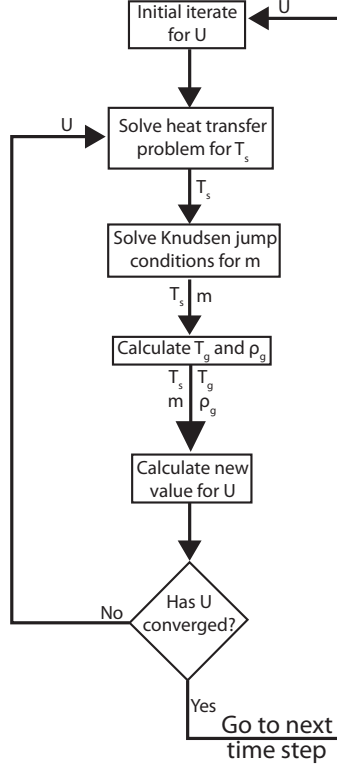


Fig. 4. Flow of the model.

The entire process of taking a new step in time can thus be viewed as finding a fixed point U such that

$$\mathfrak{F}(U) = U, \quad (25)$$

which has to be solved by an iterative method. We choose to use the secant method to solve for U , as it is a gradient free method. The code has therefore two nested iterations, one for the time step, and an inner iteration for the convergence of the secant method. In the tests below, it takes less than 5 iterations to converge to a suitable value for U , using an error tolerance of $U_{\text{TOL}} = 1 \times 10^{-8}$. Our convergence condition is $\frac{|U_c - U_+|}{U_+} < U_{\text{TOL}}$. Figure 5 illustrates the generic behavior of \mathfrak{F} at a given time. The physical solution is the smallest of the two.

In line with the simplicity of the present approach, the heat transfer problem is discretized through standard second order finite differences in space and first order backward differences in time. The spatial domain is $5 \times 10^{-4} \text{m}$ and the number of spatial nodes used below is $N = 1000$. An implicit temporal discretization is chosen for stability purposes. For the experiments at hand, a time step $\Delta t = 10^{-9} \text{sec}$ is appropriate. Since the heat transfer equation is linear, we solve it with a tridiagonal solver at each time step. To determine the value of T_s for the radial averaging methods, we average the temperature over the interface surface. To integrate the temperature, a simple numerical

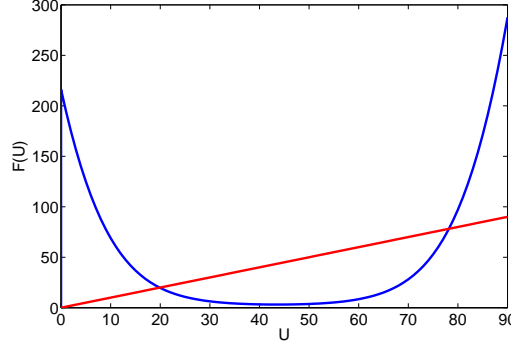


Fig. 5. Plot of the fixed point function at time $t = 1 \times 10^{-7}$ sec. The line $\mathfrak{F}(U) = U$ is also plotted to show the existence of a fixed point.

quadrature (midpoint rule) is used.

To solve for m in the Knudsen layer jump conditions, we use the Newton nonlinear solver with Armijo line search [6]. The initial iterate is taken from the value at the previous time step. With an absolute tolerance of 10^{-7} , the algorithm converges in less than 10 iterations. Until the Mach number get above 1.5, the subsonic equations are solved first; if this results in a Mach number above unity, we then solve the supersonic equations.

Finally, the aspect ratio κ needs to be determined. Denoting here by d_h and r_h the hole depth generated by one of our models and the corresponding radius, we determine κ so as to minimize

$$J(\kappa) = \left(\frac{d_h - d_{exp}}{d_{exp}} \right)^2 + \left(\frac{r_h - r_{exp}}{r_{exp}} \right)^2,$$

d_{exp} and r_{exp} being the experimental values of the hole depth and radius. We use a Nelder-Mead optimization method to minimize the above function, and it takes about 15 function evaluations to find the minimum.

4 Results

The above method is considered to simulate laser drilling in 316 stainless steel. The relevant material properties are given in Table 1.

The experimental data are taken from [5,14] where a Yb-doped fiber laser is used. Measurements using a photodiode sensor reveal that the power profile consists of an initial spike of about $1\mu s$ with an output power typically larger than the rated power of the laser, followed by a slowly decreasing quasi steady-state plateau which is lower than the rated output and lasts about $4\mu s$. This type of profile is typical of fiber lasers. The laser pulse power profile used in

density ρ_s	7500 kg/m ³	heat capacity c_s	630 J/kg K
melting temp. T_m	1400 °K	vaporization temp. T_v^*	3134 °K
thermal conductivity k_s	29 W/m K	latent heat of fusion L_f	2×10^5 J/kg
latent heat of vap. L_v^\dagger	7.6×10^6 J/kg	beam diameter	10 μ m

Table 1

Material properties of 316 stainless steel and laser parameters; the “star values” are estimated from measured values for iron, the “dagger” values are estimated from 304 stainless steel [3].

our model is an approximation of the true laser profile. Both power profiles are shown in Figure 6.

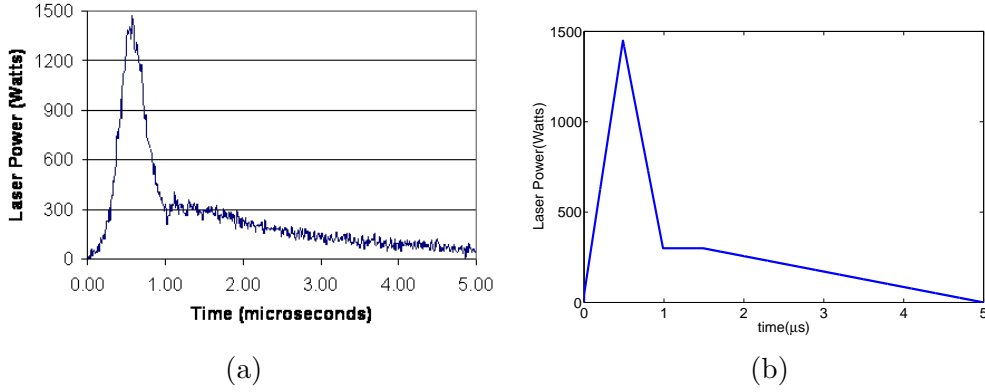


Fig. 6. (a) The true power profile used in experiment. (b) The approximate power profile used in our model.

The surface temperature of the workpiece at the vapor interface is displayed in Figure 7 for all three assumed geometries described in Section 2, i.e., conical ($\ell = 1$), parabolic ($\ell = 2$) and purely one-dimensional ($\ell \rightarrow \infty$).

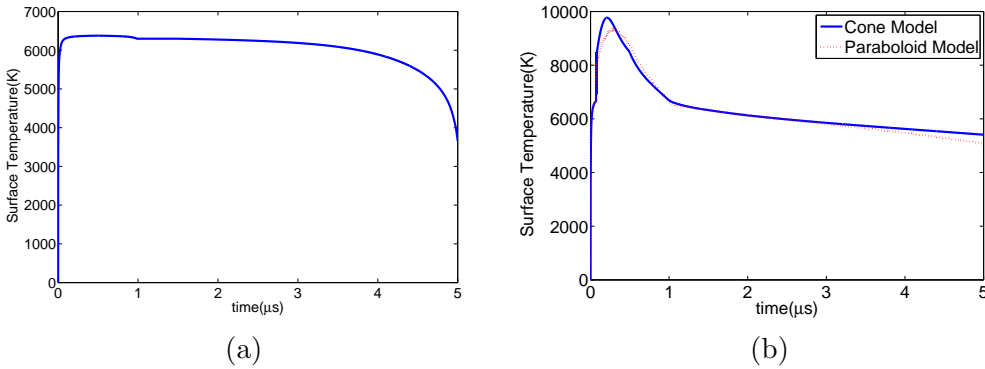


Fig. 7. The surface temperature of the workpiece(T_s) as a function of time; (a) purely one-dimensional profile ($\ell \rightarrow \infty$), (b) conical ($\ell = 1$) and parabolic profiles ($\ell = 2$).

The speed of the interface is shown in Figure 8. Significantly, the purely one-dimensional model “misses” the initial spike in velocity that the two other models predict

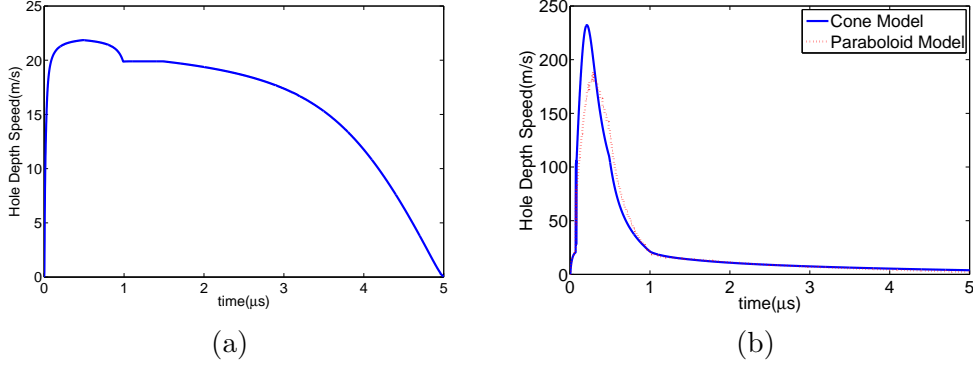


Fig. 8. The speed U of the vapor interface as a function of time; (a) purely one-dimensional profile ($\ell \rightarrow \infty$), (b) conical ($\ell = 1$) and parabolic profiles ($\ell = 2$).

Figure 9 illustrates the fact that, as mentioned in Section 2, the supersonic case applies during most of the experiment.

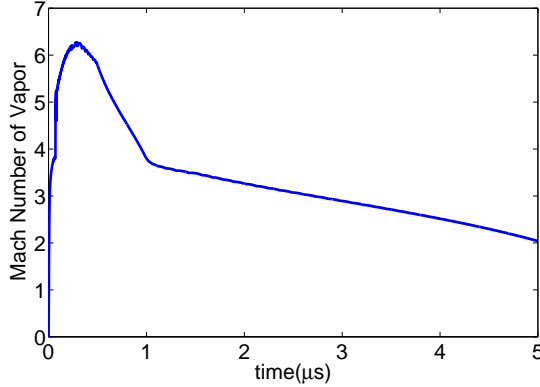


Fig. 9. Evolution of the Mach number; the flow is mostly supersonic.

The most critical aspect of the problem is the determination of the drilling depth. In the experiment considered here, the depth of the hole is measured post drilling through careful grinding of the workpiece along vertical planes until the hole is made visible. While delicate, this measurement is one of the few reliable available experimental data. Table 2 lists our results.

The position of the interface as a function of time is displayed in Figure 10. The results of the purely one-dimensional formulation ($\ell \rightarrow \infty$) underestimates the depth of the hole. The radially averaged models perform better since some of the geometry of the hole is incorporated into the model. These models also allow us to use a Gaussian profile for the laser beam, which is what is

	Hole Depth	Hole Radius
Experimental Data	136 μm	11.5 μm
One-d. profile ($\ell \rightarrow \infty$)	80 μm	
Conical profile ($\ell = 1$)	133 μm	11.1 μm
Parabolic profile ($\ell = 2$)	127 μm	10.5 μm

Table 2

Experimental and numerical results.

used experimentally. There is no significant difference between the cone and paraboloid models.

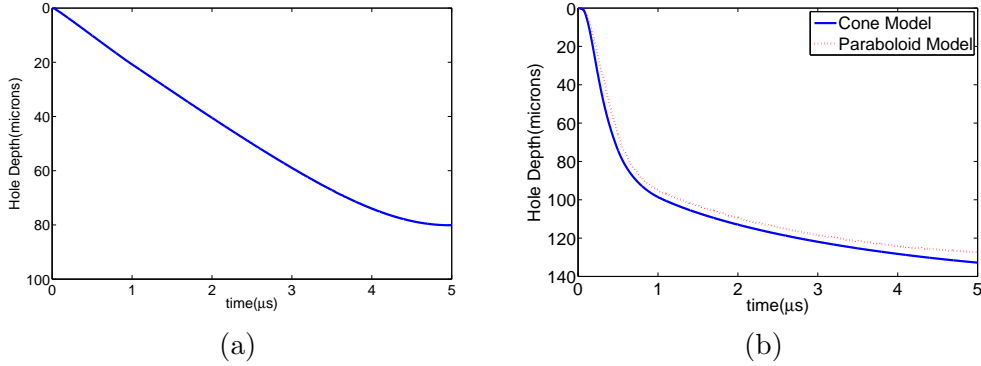


Fig. 10. Position of the vapor interface as a function of time. (a) is the two-phase model. (b) is the radially averaged models.

5 Conclusion

The proposed model, while numerically inexpensive, is in good agreement with the available data, establishing the feasibility of the proposed approach. However, additional work is needed to fully assess the extent of its range of validity. For the present type of applications, measurements are in fact quite delicate; this includes not only the measurements of state variables such as the temperature but also of physical properties such latent heat of vaporization for instance. Given this type of uncertainties, we expect Verification and Validation to play an increasing role in the future for the type of industrial applications considered here. A simple model such as the one proposed is ideal for that purpose.

References

- [1] S. ANISIMOV, *Vaporization of metal absorbing laser radiation*, Soviet Physics JETP, 27 (1968), pp. 182–183.
- [2] H.B. CALLEN, *Thermodynamics and an Introduction to Thermostatistics*, Wiley, 1985.
- [3] W.S. CHANG, S.J. NA, *A study on the prediction of the laser weld shape with varying heat source equations and the thermal distortion of a small structure in micro-joining*, J. Material Processing Tech., 120 (2002), pp. 208–214.
- [4] J.P. COLOMBIER, P. COMBIS, F. BONNEAU, R. LE HARZIC AND E. AUDOUARD, *Hydrodynamics simulations of metal ablation by femtosecond laser irradiation*, Phys. Rev. B, 71 (2005), pp. 165406-1–165406-6.
- [5] W.R. HARP, J.R. DILWITTH AND J.F. TU, *Laser ablation using a long-pulsed, high-fluence, CW single mode fiber laser*, J. Material Processing Tech., 198 (2008), pp. 22–30.
- [6] C.T. KELLEY, *Iterative methods for linear and nonlinear equations*, Frontiers in Applied Mathematics, #16, SIAM, 1995.
- [7] H. KI, P.S. MOHANTY AND J. MAZUMDER, *Multiple reflection and its influence on keyhole evolution*, J. Laser Applications, 14 (2002), pp. 39–45.
- [8] C.J. KNIGHT, *Theoretical modeling of rapid surface vaporization with back pressure*, AIAA Journal, 17 (1979), pp. 519–523.
- [9] K. LEONG, *Power drilling*, Industrial Laser Solutions, 2007, http://www.industrial-lasers.com/display_article/291963/39/none/none/Feat/Power-drilling
- [10] R.L. LEVEQUE, *Finite Volume Methods for Hyperbolic Problems*, Cambridge University Press, 2002.
- [11] D.K.Y. LOW, L. LI AND P.J. BYRD, *Hydrodynamic physical modeling of laser drilling*, Trans. ASME, 124 (2002), pp. 852–862.
- [12] V.I. MAZHUKIN, M.G. LOBOK AND B. CHICHKOV, *Modeling of fast transitions dynamics in metal target irradiated by pico- and femtosecond pulsed laser*, Appl. Surf. Sc., 255 (2009), pp. 5112–5115.
- [13] V.V. SEMAK AND A. MATSUNAWA, *The role of recoil pressure in energy balance during laser processing*, J. Phys. D: Appl. Phys., 30 (1997), pp. 2541–2552.
- [14] J. TU, *Personal communication*, Dept. of Aerospace and Mechanical Engineering, North Carolina State University, 2008.
- [15] K. VERHOEVEN, *Modelling Laser Percussion Drilling*, PhD, Technische Universiteit Eindhoven, 2004.
- [16] T. YTREHUS AND S. ØSTMO *Kinetic Theory Approach to Interphase Processes*, Int. J. of Multiphase flow, 22 (1996), pp. 133–155.